

# The stability number as a metric for electrocatalyst stability benchmarking

Simon Geiger<sup>1,7\*</sup>, Olga Kasian<sup>1,7</sup>, Marc Ledendecker<sup>1</sup>, Enrico Pizzutilo<sup>1</sup>, Andrea M. Mingers<sup>1</sup>, Wen Tian Fu<sup>2</sup>, Oscar Diaz-Morales<sup>2</sup>, Zhizhong Li<sup>3</sup>, Tobias Oellers<sup>4</sup>, Luc Fruchter<sup>3</sup>, Alfred Ludwig<sup>4</sup>, Karl J. J. Mayrhofer<sup>1,5,6</sup>, Marc T. M. Koper<sup>2</sup> and Serhiy Cherevko<sup>1,5\*</sup>

**Reducing the noble metal loading and increasing the specific activity of the oxygen evolution catalysts are omnipresent challenges in proton-exchange-membrane water electrolysis, which have recently been tackled by utilizing mixed oxides of noble and non-noble elements. However, proper verification of the stability of these materials is still pending. Here we introduce a metric to explore the dissolution processes of various iridium-based oxides, defined as the ratio between the amounts of evolved oxygen and dissolved iridium. The so-called stability number is independent of loading, surface area or involved active sites and provides a reasonable comparison of diverse materials with respect to stability. The case study on iridium-based perovskites shows that leaching of the non-noble elements in mixed oxides leads to the formation of highly active amorphous iridium oxide, the instability of which is explained by the generation of short-lived vacancies that favour dissolution. These insights are meant to guide further research, which should be devoted to increasing the utilization of highly durable pure crystalline iridium oxide and finding solutions to stabilize amorphous iridium oxides.**

Electrochemical water splitting is considered to play a key role in the new energy scenario to produce hydrogen, acting as a central energy carrier and as a raw material for the chemical industry. Still, the persistent challenges of this concept are: the slow kinetics of the oxygen evolution reaction (OER); and the need for expensive materials as catalysts or related components. Especially for proton-exchange-membrane electrolysis, the acidic environment together with high anodic potentials limits the choice of catalyst materials to expensive noble metals. The best-known catalysts for OER contain high amounts of scarce iridium that hampers large-scale implementation of this technology. Smart catalyst design is needed to decrease noble metal loadings and increase specific activity and stability.

Various iridium-based mixed oxides<sup>1–8</sup> have been investigated as potential catalyst material to tackle the mentioned challenges by increased specific activity and lower percentage of noble metals. Enhanced activity and apparently decent stability were demonstrated in comparison to IrO<sub>2</sub>, Ir-black and other benchmark materials. However, the stability aspect needs more rigorous investigation. In particular, non-noble alkali or rare-earth elements are expected to be thermodynamically unstable in acidic electrolytes<sup>9</sup>, favouring the formation of amorphous iridium oxide structures after leaching. These structures have been shown to degrade significantly in acidic electrolyte during OER<sup>10–12</sup>, accentuating the need for further understanding of degradation processes.

The most prominent examples are iridium-based perovskites recently investigated in acidic electrolyte<sup>1,2</sup>. An important early discussion of this material class may be found in ref. <sup>13</sup>. Since then, numerous studies on the use of perovskites for alkaline water splitting have been published<sup>14,15</sup>. Exceptionally high OER activities were

achieved, for example, by varying the occupancy of 3d orbitals of surface transition metals<sup>14</sup> or tuning oxygen vacancies by means of straining<sup>16</sup>. However, several groups brought up the important aspect of surface amorphization during OER<sup>17–20</sup>. Ref. <sup>17</sup> indicated that especially those materials with high amorphization are the ones that show high activity, expressing the need for further investigations on the number of involved active sites. More so in acidic environments, catalyst stability and amorphization can be an issue. Therefore, a thorough investigation of specific activity and dissolution processes of iridium-based perovskites in 0.1 M HClO<sub>4</sub> is presented in this work.

In general, contemporary challenges to explore new electrocatalysts are, in addition to increased activity: the determination of the real electrochemical surface area by identification and quantification of the active sites, enabling a reliable comparison of different materials; and the investigation of degradation by thorough quantification of dissolution products, assuming dissolution as major degradation process of electrocatalysts. Both parameters are important indicators of an electrocatalyst's performance. Our study aims to fill these important gaps by electrochemical quantification of active centres for OER and in situ dissolution analysis by combining a scanning flow cell (SFC) with inductively coupled plasma mass spectrometry (ICP-MS). The amount of dissolved iridium is presented in relation to the evolved oxygen as an independent metric called the stability number (S-number). The latter is beneficial to estimate lifetimes and, together with online electrochemical mass spectrometry (OLEMS), underlines the proposed dissolution mechanisms of the investigated materials, namely double perovskite powders with A<sub>2</sub>BIrO<sub>6</sub> structure (A = Ba, Sr; B = Nd, Pr, Y), amorphous IrO<sub>x</sub> powder, crystalline IrO<sub>2</sub> powder, SrIrO<sub>3</sub> perovskite films,

<sup>1</sup>Department of Interface Chemistry and Surface Engineering, Max-Planck-Institut für Eisenforschung GmbH, Düsseldorf, Germany. <sup>2</sup>Leiden Institute of Chemistry, Leiden University, Leiden, the Netherlands. <sup>3</sup>Laboratoire de Physique des Solides, CNRS, Université Paris-Sud, Orsay, France. <sup>4</sup>Institute for Materials, Ruhr-Universität Bochum, Bochum, Germany. <sup>5</sup>Helmholtz-Institute Erlangen-Nürnberg for Renewable Energy (IEK-11), Forschungszentrum Jülich GmbH, Erlangen, Germany. <sup>6</sup>Department of Chemical and Biological Engineering, Friedrich-Alexander-Universität Erlangen-Nürnberg, Erlangen, Germany. <sup>7</sup>These authors contributed equally: Simon Geiger, Olga Kasian. \*e-mail: [geiger@mpie.de](mailto:geiger@mpie.de); [s.cherevko@fz-juelich.de](mailto:s.cherevko@fz-juelich.de)

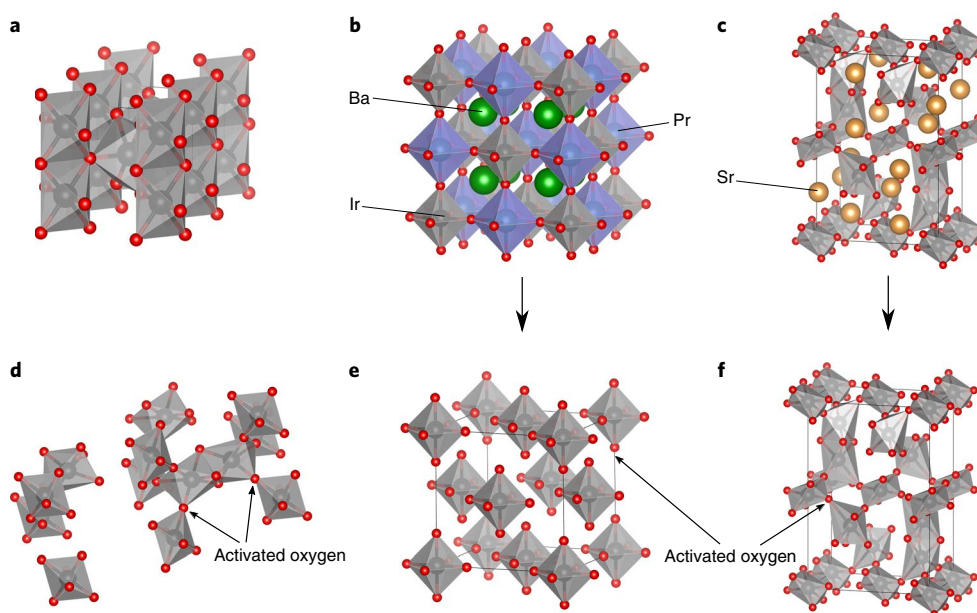


**Fig. 1 | Crystal structure of the investigated materials.** **a**, Rutile  $\text{IrO}_2$ . **b**, An example of a B-site-ordered double perovskite ( $\text{Ba}_2\text{PrIrO}_6$ ). **c**, A single perovskite with alternating cubic and hexagonal layers ( $\text{SrIrO}_3$ ). **d**, Assumed structure of amorphous iridium oxide; gaps are filled with intercalated water molecules (not shown). **e**, A leached double perovskite showing isolated  $\text{IrO}_6$  octahedra, which will collapse into an amorphous structure. **f**, A leached  $\text{SrIrO}_3$  resulting in an anatase-like iridium oxide structure.

electrochemically formed hydrous  $\text{IrO}_x$  films and crystalline  $\text{IrO}_2$  films. A general perspective on the applicability of the mentioned iridium oxide structures towards acidic water splitting is presented.

## Results

**Leaching processes in perovskites.** The information on the catalyst surface composition is essential for understanding electrochemical reactions at the catalyst/electrolyte interface. Therefore, before going into the mechanistic analysis, the dissolution behaviour of all materials was investigated during initial contact with 0.1 M  $\text{HClO}_4$  at open-circuit potential. While crystalline  $\text{IrO}_2$  and amorphous  $\text{IrO}_x$  do not dissolve initially, perovskites do undergo intensive leaching. First, the non-noble elements (Ba, Sr, Nd, Pr and Y) dissolve as expected from available thermodynamic data for single elements<sup>9</sup> and related experimental works<sup>1,2</sup>. Moreover, in double perovskites, we observed dissolution of iridium in the range of 30–40 w% from the initial value during 60 s of contact at open-circuit potential (see Supplementary Table 1 and Supplementary Fig. 1). This can be explained on the basis of the crystal structure illustrated in Fig. 1b. As the component B (for example, Pr) is part of the lattice, leaching of B goes hand-in-hand with the generation of isolated  $\text{IrO}_6$  octahedra, which are prone to dissolve in parallel. Furthermore, we expect that the structure will collapse and reform in an amorphous iridium oxide. To underline this statement, one exemplary material of the double perovskite family was examined during a prolonged leaching experiment. Energy-dispersive X-ray spectroscopy (EDS) analysis confirms complete removal of Ba and Pr after keeping the powder for 14 days in 0.1 M  $\text{HClO}_4$ , leaving behind an amorphous iridium oxide structure. This structure is demonstrated by selected-area electron diffraction (SAED) in Supplementary Fig. 2.

Single perovskites, on the other hand, consist of a coherent iridium oxide structure with intercalated non-noble elements (see Fig. 1c). Thus, initial dissolution of a 20 nm  $\text{SrIrO}_3$  film mainly affects Sr (3.0 w%). The leftover backbone of iridium oxide equals an anatase structure<sup>1,21</sup> and dissolves less (0.01 w%). Since no stable anatase phase of iridium oxide has been reported to the best of our knowledge, it is highly probable that the structure will collapse as

well into amorphous iridium oxide. Similar cyclic voltammogram (CV) shapes of electrochemically grown hydrous  $\text{IrO}_x$  and leached  $\text{SrIrO}_3$  support this assumption. Further details on leaching and dissolution can be found in Supplementary Fig. 3.

**The oxide structure and its relevance for activity and dissolution.** To understand the observed results on activity and stability presented later in the manuscript, we continue with a discussion on oxide structures and oxidation states before and after the initial leaching process. In Fig. 1, the structures of rutile  $\text{IrO}_2$ , amorphous  $\text{IrO}_x$ , a double perovskite ( $\text{Ba}_2\text{PrIrO}_6$ ) and a single perovskite ( $\text{SrIrO}_3$ ) are presented. The dense packing and edge-sharing oxygen of the octahedra in the rutile structure are in contrast to the loose packing and corner-sharing octahedra in  $\text{Ba}_2\text{PrIrO}_6$  and  $\text{SrIrO}_3$ , generating lower-coordinated oxygen atoms (activated oxygen). Leaching of the non-noble elements A and B in  $\text{A}_2\text{BIrO}_6$  destroys the crystal structure of the double perovskite and pure octahedral elements are linked together randomly inducing a high number of accessible activated oxygen atoms and vacancies. Similar structures can be achieved by leaching Sr from  $\text{SrIrO}_3$  or Ni from  $\text{IrNiO}_x$  (ref. 3). Moreover, classical potential cycling of iridium metal<sup>22</sup> and mild calcination of iridium precursors<sup>23</sup> are optional preparation methods.

The binding energies of the 4f electrons of iridium and the 1s electrons of oxygen obtained via X-ray photoemission spectroscopy (XPS) were utilized to further analyse the chemical environment of iridium and oxygen in the structure. On the basis of a computational model, ref. 24 studied the formation of an iridium vacancy in a supercell. According to the calculations, this leads to the formation of  $\text{O}^{\cdot-}$  and  $\text{Ir}^{\text{III}}$  species, as supported by XPS and X-ray absorption spectroscopy investigations. Hereby, the authors explained the positive shift of the Ir 4f binding energy<sup>24</sup> in amorphous  $\text{IrO}_x$ , which is shown in Fig. 2a. The Ir 4f peak of  $\text{Ba}_2\text{PrIrO}_6$  is shifted to even higher binding energies; however, the pristine structure rather indicates the presence of  $\text{Ir}^{\text{V}}$ , which would result in a similar peak shift<sup>25</sup>. Still, another study<sup>26</sup> reported a  $\text{Pr}^{\text{IV}}/\text{Ir}^{\text{IV}}$  couple present in  $\text{Ba}_2\text{PrIrO}_6$ , which is against the previous assumption. Consequently,

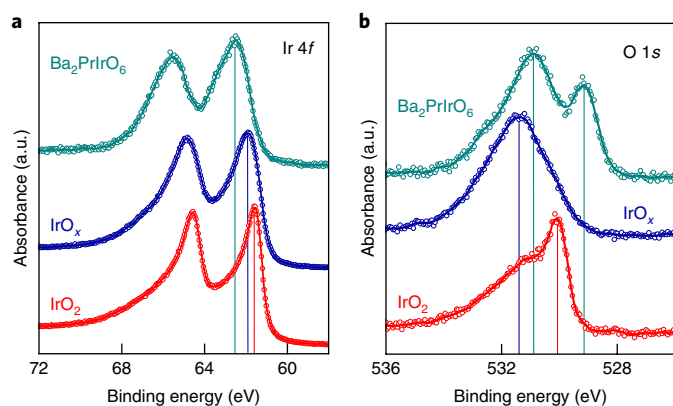


**Fig. 2 | XPS results for pristine  $\text{Ba}_2\text{PrIrO}_6$ , amorphous  $\text{IrO}_x$  and crystalline  $\text{IrO}_2$ .** **a**, Ir 4f spectra. **b**, O 1s spectra. Additional results for the leached  $\text{Ba}_2\text{PrIrO}_6$  are presented in Supplementary Fig. 2.

based on XPS data alone, a clear statement on the oxidation states is difficult. However, XPS clearly expresses the different environment of the iridium atoms in the respective structures. After leaching of  $\text{Ba}_2\text{PrIrO}_6$  in 0.1 M  $\text{HClO}_4$ , the spectrum is very similar to that of amorphous iridium oxide (see Supplementary Fig. 2c,d). This observation could be understood as a decreased amount of  $\text{Ir}^{\text{VI/V}}$  and the formation of  $\text{Ir}^{\text{III}}$  by intensive leaching and the creation of vacancies, similar to the theoretical model mentioned earlier in this section.

The O 1s spectra in Fig. 2b confirm that exclusively crystalline  $\text{IrO}_2$  contains oxygen atoms in the rutile lattice at a binding energy of  $\sim 530$  eV. In perovskites and amorphous oxide, the binding energy of the main peak is shifted to positive values, which is usually assigned to hydroxyl groups<sup>3</sup>. Alternatively, it could be attributed to oxygen atoms with a different environment (for example, activated oxygen atoms). The shoulder at 529 eV for  $\text{Ba}_2\text{PrIrO}_6$  results from lattice oxygen bound to the Pr atom<sup>2</sup> and disappears after extensive leaching (see Supplementary Fig. 2d). Similar absorption features were observed in  $\text{IrNiO}_x$  (ref.<sup>3</sup>) and explained by ‘oxygen hole’ states induced by substitution of  $\text{Ir}^{\text{IV}}$  with  $\text{Ni}^{\text{II}}$  (ref.<sup>27</sup>). We suggest that the presence of activated oxygen atoms is crucial for the explanation of the following results on OER activity and dissolution.

**Stability and activity with respect to OER.** The SFC coupled to ICP-MS analytics enables in situ detection of dissolved iridium ions during oxygen evolution. This approach was used to investigate film and powder materials by performing a linear sweep of potential at  $5 \text{ mV s}^{-1}$ , illustrated in Fig. 3. Potential and dissolution are plotted on the same timescale. The insets present the integrated amount on a logarithmic scale. In line with previous reports, we recorded orders of magnitude higher dissolution for metallic iridium and hydrous iridium oxide in comparison to crystalline iridium oxide<sup>10,28,29</sup>. Perovskites, additionally studied in this work, also show high dissolution in the range of amorphous/hydrous oxide and therefore might not be suitable for long-term operation. Still, its high activity, demonstrated in the following, is of importance to understand the clues on the synthesis of an improved OER catalyst.

To take into account the different active surface areas of the samples, the OER current is normalized to the pseudocapacitive charge  $Q_{\text{oxide}}$  extracted from features in the CVs (see Fig. 4b).  $Q_{\text{oxide}}$  is considered as a fair approximation<sup>30</sup> for the number of involved active sites, avoiding misinterpretation of data on activity due to surface area effects. On the basis of the position of the redox peak, we assume that predominantly  $\text{Ir}^{\text{IV}}/\text{Ir}^{\text{V}}$  transition<sup>31,32</sup> appears in double perovskites while  $\text{Ir}^{\text{III}}/\text{Ir}^{\text{IV}}$  is suppressed. In commercial

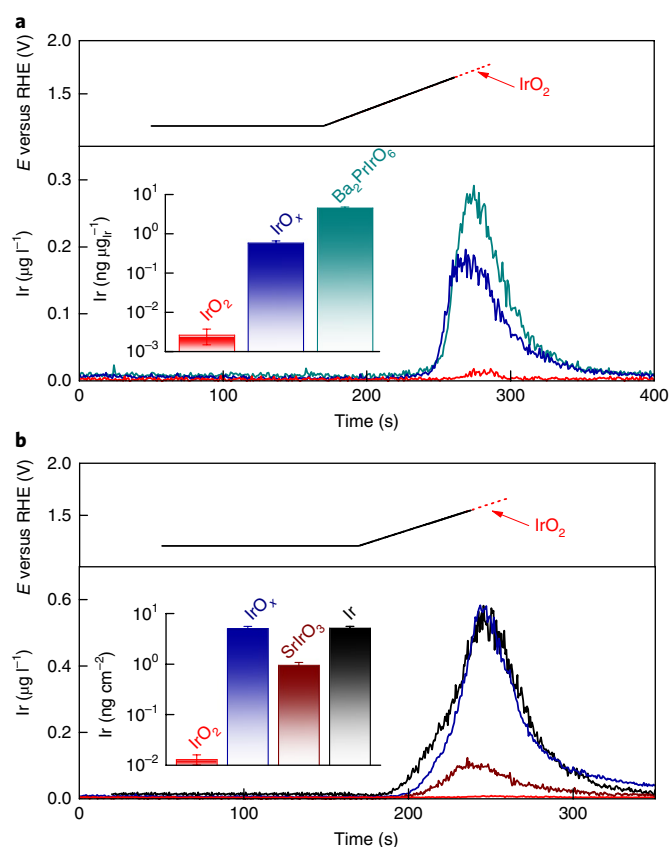


**Fig. 3 | Investigation of iridium dissolution during OER.** **a**, Detected iridium concentration in the electrolyte during the second linear scan of potential to 1.65 V versus the reversible hydrogen electrode (RHE) for the investigated powders. In the case of  $\text{IrO}_2$ , a higher loading was used and the potential was increased to 1.8 V versus the RHE to reach iridium concentrations above the detection limit of the ICP-MS. Inset: integrated dissolution normalized by the actual mass of iridium loaded given in nanograms per microgram of iridium. **b**, Detected iridium concentration in the electrolyte during a linear scan of potential to 1.55 V versus the RHE for the investigated films. In the case of  $\text{IrO}_2$ , the potential was increased to 1.65 V versus the RHE. Inset: integrated dissolution normalized to the geometric surface area given in nanograms per square centimetre. All error bars were obtained by standard deviation of at least three independent repetitions of the measurements.

amorphous  $\text{IrO}_x$ , the  $\text{Ir}^{\text{III}}/\text{Ir}^{\text{IV}}$  redox peak is much more pronounced with a second wave indicating further oxidation to  $\text{Ir}^{\text{V}}$ . Considering the normalized OER currents, it can be stated that double perovskites obtain the highest intrinsic activity, which is assigned to numerous activated oxygen atoms resulting from complete isolation of  $\text{IrO}_6$  octahedra after leaching. Further details on mass-normalized OER activity and scanning electron images can be found in Supplementary Figs. 4–6.

In Fig. 4c,d, the analogous procedure is illustrated for sputtered samples. The low roughness of these films allows normalization to geometric surface area. Exceptions are leached  $\text{SrIrO}_3$  and electrochemically grown hydrous iridium oxide, investigated numerous in the literature<sup>22,33,34</sup>. Both show enhanced pseudocapacitance assigned to the formation of a porous hydrous oxide layer. Almost identical CV shapes are indications of very similar structures. The extraordinary activity of these porous 3D structures is, inter alia, related to the high number of accessible active sites. Normalization to pseudocapacitive charge, as mentioned for

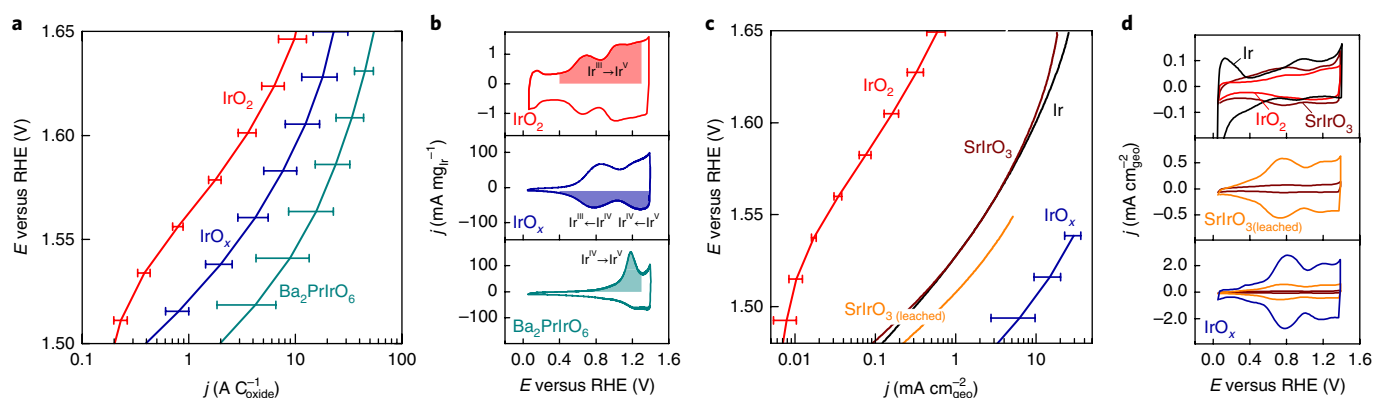


**Fig. 4 | Comparison of the investigated materials in terms of activity.** **a**, OER activity of the powder materials recorded with a linear scan of potential at  $5\text{ mV s}^{-1}$  (iR-drop corrected). The current is normalized to the pseudocapacitive charge in the CVs. **b**, CVs recorded with  $200\text{ mV s}^{-1}$ ; the integrated area of the oxide charge used for normalization is highlighted. **c**, OER activity of the investigated films recorded with a linear scan of potential at  $5\text{ mV s}^{-1}$ . The current is normalized to the geometric surface area. **d**, CVs recorded with  $200\text{ mV s}^{-1}$ . All measurements were carried out in  $0.1\text{ M HClO}_4$  purged with argon. All error bars were obtained by standard deviation of at least three independent measurements.

powder samples, is necessary to reveal further insights into the specific activity. The observed trend for specific activity is:  $\text{Ba}_2\text{PrIrO}_6 > \text{SrIrO}_3 = \text{IrO}_x > \text{IrO}_2$ , presented and discussed in Supplementary Note 3 and Supplementary Figs. 7 and 8. Focusing on the flat samples of iridium metal, crystalline  $\text{IrO}_2$  and pristine  $\text{SrIrO}_3$  with similar  $Q_{\text{oxide}}$  (Fig. 4d), one can conclude a two orders of magnitude higher specific OER activity on  $\text{SrIrO}_3$  and metallic iridium in comparison to crystalline  $\text{IrO}_2$ , caused by a thin hydrated oxide layer formed on  $\text{SrIrO}_3$  via leaching and metallic iridium via surface oxidation during OER<sup>33</sup>, which is not present for crystalline iridium oxide.

**Mechanistic insights.** With the gained understanding on structure, dissolution and activity, we want to combine existing mechanisms of the OER on iridium-based catalysts<sup>35–39</sup> with a mechanism for simultaneous dissolution. The starting point is the differentiation of two oxygen species present either in crystalline iridium oxide or amorphous, hydrated iridium oxides and the significantly higher stability of the crystalline structure in comparison to the amorphous, hydrated structure as presented in Fig. 3.

The case of amorphous hydrous oxide and, hence, leached perovskites, merits special attention, as its structure is still unknown. According to a previous study<sup>40</sup>, its enhanced activity is caused by electrophilic  $\text{O}^{1-}$  species that are preferred for nucleophilic attack by water, reducing the activation energy for the adsorption. Another study<sup>20</sup> came to similar conclusions using  $\text{La}_2\text{LiIrO}_6$  as a model catalyst. There are several indications that the activated oxygen atoms as described in this work and the above-mentioned ‘ $\text{O}^{1-}$  species’ are indeed interchangeable. The presence of  $\text{O}^{1-}$  is, however, counterintuitive, as the high electronegativity of oxygen in comparison to iridium should hardly allow the allocation of a formal oxidation state of  $-1$ . On the basis of structural investigation of different amorphous iridium oxides, Willinger et al.<sup>41</sup> concluded that the ratio between corner- and edge-sharing  $\text{IrO}_6$  octahedra is determining the OER activity. Thus, a high number of corner-sharing oxygen atoms (activated oxygen) facilitates the OER. Regardless of the formal oxidation state and termination, it was experimentally proven by  $^{18}\text{O}$  labelling for Co-based perovskites that activated oxygen can participate in the OER, which was taken as evidence for oxygen redox chemistry<sup>38</sup>. Furthermore, it is an important argument to explain the instability of amorphous iridium oxides. In the following, the term lattice oxygen accounts generally for all oxygen atoms that are part of the structure and is not exclusively limited to the described oxygen atoms of the rutile lattice.

Evidence for lattice oxygen participation during OER on iridium oxides is rare<sup>42</sup>. To resolve its extent on rutile and amorphous iridium oxides in more detail, a method of isotope labelling combined with OLEMS was used. The labelled  $\text{Ir}^{18}\text{O}_2$  and  $\text{Ir}^{18}\text{O}_x$  films (for preparation, see Methods) were polarized galvanostatically in  $\text{H}_2^{16}\text{O}$ -based electrolyte and the formation of volatile species with mass-to-charge ratios of 32 ( $^{16}\text{O}^{16}\text{O}$ ), 34 ( $^{16}\text{O}^{18}\text{O}$ ) and 36 ( $^{18}\text{O}^{18}\text{O}$ ) was measured online (see Fig. 5). To compensate for the influence of naturally occurring  $\text{H}_2^{18}\text{O}$  isotopes in the  $\text{H}_2^{16}\text{O}$ -based electrolyte, the same protocol was applied to unlabelled rutile  $\text{Ir}^{16}\text{O}_2$  and hydrous  $\text{Ir}^{16}\text{O}_x$  prepared by identical procedures. During anodic polarization, both labelled and unlabelled rutile samples show similar formation of various oxygen products. This indicates that participation of lattice oxygen in the OER is absent or negligible. In contrast, the formation of species with  $m/z=34$  and  $m/z=36$  on  $\text{Ir}^{18}\text{O}_x$  is more intense in comparison to the unlabelled sample (Fig. 5b,c), denoting the instability of amorphous oxide lattice towards OER. However, the low measured intensities of  $m/z=34$  and  $m/z=36$  suggest that the major part of the evolved oxygen molecules is formed via water discharge. Gradual decrease of  $m/z=34$  and  $m/z=36$  signals on labelled  $\text{Ir}^{18}\text{O}_x$  indicates an exchange between lattice oxygen atoms and oxygen from water induced by the OER.

On the basis of the results shown in Fig. 5 and additional data presented in the literature, we propose a summarized view of the OER mechanisms in Fig. 6. Figure 6a shows the classical mechanism for crystalline iridium oxide, the adsorbate evolution mechanism<sup>35–37</sup>. The reaction can happen either on a single iridium site via an OOH intermediate<sup>25,43</sup> (acid–base)<sup>36,44</sup> or by the coupling of two oxygen atoms from different sites (direct coupling)<sup>45</sup>. The cycle in Fig. 6b is based on previously proposed mechanisms<sup>37,38,46</sup>. Here, the reaction pathway differs by participation of activated lattice oxygen in the reaction. It is assumed to be operative in the case of amorphous  $\text{IrO}_x$  and in leached perovskites. The activated oxygen is attacked by water (step 2) and removed as  $\text{O}_2$  from the surface (step 3) leaving behind an oxygen vacancy<sup>37,38,47</sup>. This can happen either with one lattice oxygen or by combining two lattice oxygen atoms as shown in Fig. 5c, leading in both cases to an iridium atom with weakened bonding, which has a higher probability to dissolve. This scenario is less likely to happen for crystalline oxide. Participation of lattice oxygen, if at all, is restricted to the outer surface while bulk oxygen will not participate and maintain a high coordination of the iridium atom, resulting in a significantly lower probability of the iridium atom dissolving out of the structure. In contrast, for porous hydrous oxides with

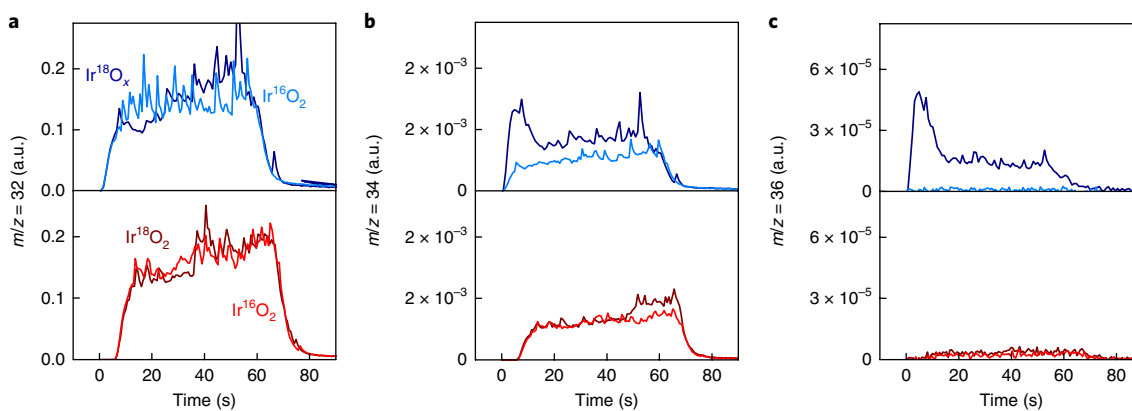


**Fig. 5 | Online observation of lattice oxygen evolution.** **a–c**, Intensities of  $m/z = 32$  (**a**),  $34$  (**b**) and  $36$  (**c**) for rutile  $\text{Ir}^{18}\text{O}_2/\text{Ir}^{16}\text{O}_2$  and hydrous  $\text{Ir}^{18}\text{O}_x/\text{Ir}^{16}\text{O}_x$  films during 60 s of anodic polarization at  $25 \text{ mA cm}^{-2}_{\text{geo}}$ . The signals from  $m/z$  of 32, 34 and 36 correspond to  $^{32}\text{O}_2$ ,  $^{34}\text{O}_2$  and  $^{36}\text{O}_2$ , respectively. Electrolyte:  $0.1 \text{ M HClO}_4$  in  $\text{H}_2^{16}\text{O}$ . The measured potential at the end of the polarization was 1.8 and 1.87 V versus the RHE for  $\text{IrO}_x$  and  $\text{IrO}_2$ , respectively.

intercalated water molecules, iridium atoms inside the structure can participate in the reaction.

Whereas the probability of dissolution is still very low, in most cases vacancies are refilled by adsorption of water or bulk oxygen migration<sup>20</sup> closing the catalytic cycle (step 1). We suggest that the lower activation energy for the adsorption of water in vacancies is further contributing to the higher activity of amorphous oxide structures. Dissolution itself might take place without electron transfer  $\text{Ir}^{\text{III}}_{(\text{oxide})} \rightarrow \text{Ir}^{3+}_{(\text{aq})}$ . A similar reaction pathway was proposed recently by our group, in which the existence of an  $\text{Ir}^{\text{III}}$  intermediate in the OER cycle was linked to the dissolution of hydrous iridium oxide<sup>48</sup>. Alternatively, additional electron transfer would lead to formation of  $\text{IrO}_3$  and  $\text{IrO}_4^{2-}$ , described elsewhere<sup>49,50</sup>.

As crystalline iridium oxide is assigned to the adsorbate evolution mechanism, its very low but still measurable dissolution is not considered, yet. The constancy of the S-number presented in the following section (Fig. 7c) suggests a direct relation between the OER mechanism and the dissolution mechanism. The origin of the crystalline iridium oxide dissolution might be some limited lattice oxygen participation on the surface similar to the mechanism in Fig. 5b

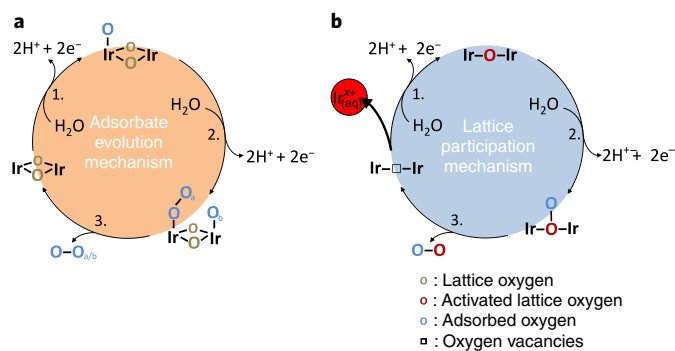


**Fig. 6 | Sketch of the simplified OER reaction mechanism with dissolution pathways.** **a**, The classical mechanism for crystalline  $\text{IrO}_2$  without participation of lattice oxygen. Two possible pathways are presented: single site and double site. **b**, The mechanism suggested for amorphous iridium oxide and leached perovskites with participation of activated oxygen in the reaction forming oxygen vacancies. Weakening the binding of iridium in the structure is taken as the main reason for the enhanced dissolution. To complete the cycle, vacancies can be filled again by adsorption of water. The octahedral configuration of iridium is not presented completely, and nucleophilic attack of water and proton removal are merged into one step to avoid overcrowding the scheme.

or other intermediates and dissolution pathways (for example, formation of volatile  $\text{IrO}_3$ )<sup>49,50</sup>.

In conclusion, a catalyst's stability is determined by: the ratio between the two presented mechanisms (a less stable material has a higher rate in the lattice participation mechanism); and the stability of the intermediate itself, which can be higher for a rutile structure in comparison to the amorphous oxide due to a more compact structure.

**The S-number and lifetime of catalysts.** Significantly higher dissolution rates of iridium, but also higher OER rates were observed for amorphous  $\text{IrO}_x$  and perovskites in comparison to crystalline  $\text{IrO}_2$ . To take into account the possible effect of the much higher amount of oxygen formed on amorphous and perovskite structures on dissolution, we introduce a metric characterizing the activity versus stability performance of a given catalyst. The so-called S-number is defined as the ratio between the amount of evolved oxygen (calculated from  $Q_{\text{total}}$ ) and the amount of dissolved iridium (extracted from ICP-MS data). The S-number describes how many oxygen molecules are formed per iridium atom lost into the electrolyte. Consequently, it is independent of the amount of involved active sites, surface area or catalyst loading and gives an illustrative comparison of the stability of various materials. Moreover, unlike current efficiency, the S-number can be calculated without knowing the exact nature of the dissolved species and can be applied to neutral species. The higher the number, the more stable the active centre of the electrocatalyst. Interestingly, a similar activity–stability factor was independently proposed while this work was underway<sup>51</sup>. Based on the dissolution measurements presented in Fig. 3, the highest S-numbers were calculated for crystalline  $\text{IrO}_2$  (Supplementary Fig. 9). Perovskite-based iridium oxides possess the lowest S-numbers with two orders of magnitude less oxygen evolved per dissolved iridium compared to rutile  $\text{IrO}_2$ . However, the influence of initially dissolved iridium from defects as well as possible stabilization during longer operation should not be overlooked in these short measurements (see the discussion in Supplementary Note 4). Hence, longer time intervals were applied as described below.

To gain a further understanding of the possible correlations of the OER mechanism and the dissolution mechanism, we varied the current per mass of iridium using galvanostatic steps of  $\sim 5$ –20 min until a steady dissolution rate was observed (see Supplementary Fig. 11). According to Fig. 7a, the S-numbers match the ones presented in Supplementary Fig. 9, which are based on a short linear scan of potential. Over a wide range of current densities ( $0.01$  to  $1 \text{ A mg}_{\text{Ir}}^{-1}$ ), constant S-numbers were observed, indicating a direct relation between oxygen evolution and dissolution for all materials.

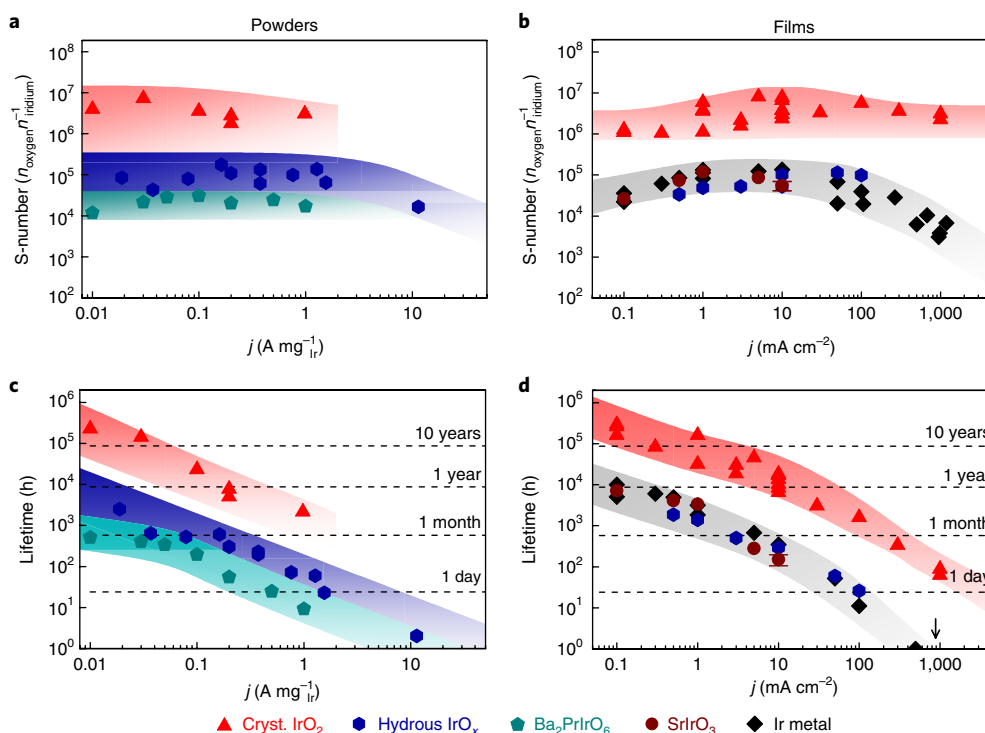


**Fig. 7 | Investigation of S-number and lifetime depending on the current load.** **a,b**, S-number plotted versus mass specific current density for powders (**a**) and geometric current density for sputtered films (**b**). Ba<sub>2</sub>PrIrO<sub>6</sub> was leached for five days in advance. **c,d**, Calculation of the catalyst's lifetime, based on equation 1 (see Methods) for powders (**c**) and films (**d**). This approach assumes steady-state dissolution and neglects increased dissolution towards the end of life due to loss of surface area. In the case of powder materials,  $m$  equals the mass of loaded iridium. In the case of films,  $m$  was set to 50  $\mu\text{g}_{\text{Ir}} \text{cm}^{-2}$ , which equals film thicknesses of about 100 nm SrIrO<sub>3</sub>, 50 nm IrO<sub>2</sub> and 20 nm iridium metal. Measurements were carried out in 0.1 M HClO<sub>4</sub>.

The difference in the absolute value of the S-number for different materials can be assigned to: a weaker bonding of the lattice oxygen in amorphous structures compared to crystalline ones, enabling a direct participation in the OER with the formation of metastable, activated iridium complexes that are more prone to dissolution; the amount of activated oxygen atoms surrounding one iridium centre, which is assumed to be higher in the case of leached Ba<sub>2</sub>PrIrO<sub>6</sub> (see Fig. 1e) in comparison to amorphous iridium oxides and rutile IrO<sub>2</sub>, elevating the chance for the occurrence of unstable iridium centres with two oxygen vacancies, caused by recombination of two activated oxygen atoms<sup>38</sup>.

The trends for sputtered films in Fig. 7b resemble the ones observed for powders. Additionally, S-numbers for sputtered metallic iridium are presented, which drop at current densities above 50 mA cm<sup>-2</sup>. A similar trend was observed for IrO<sub>x</sub> in Fig. 7a. The reason is the onset of a second dissolution pathway forming IrO<sub>4</sub><sup>2-</sup>, which is expected to occur at potentials >1.8 V versus the reversible hydrogen electrode (RHE)<sup>9</sup> (see Supplementary Fig. 12). Through kinetic stabilization, this pathway is successfully suppressed for rutile IrO<sub>2</sub> at even higher potentials (reported as well for oxide reduction in the hydrogen region<sup>28</sup>). For metallic iridium and amorphous iridium oxide, a self-accelerating degradation process can be observed when a critical current density is reached by insufficient loading or degraded catalyst. The degradation of IrO<sub>2</sub>, however, is exclusively linked to the amount of oxygen evolved and not to the applied potential.

The constancy of the S-number, observed over a wide range of current densities, indicates a relation of evolved oxygen and dissolved iridium independent on the current load and therefore also allows a relation of dissolution and lifetime of the catalyst, demonstrated in Fig. 7c,d (see equation (1) in Methods). Hereby, lifetimes

of a few days (Ba<sub>2</sub>PrIrO<sub>6</sub>), one month (IrO<sub>x</sub>) and one year (IrO<sub>2</sub>) were obtained when considering a constant current density of 0.2 A mg<sub>Ir</sub><sup>-1</sup>. Note, these findings are specific for the electrochemical cell used. Lifetimes in a proton-exchange-membrane system can deviate, as discussed in more detail in Supplementary Fig. 13.

## Conclusion

In this work, the S-number is introduced as a metric for stability benchmarking of electrocatalysts, enabling illustrative and fast comparison of stability properties, direct evaluation of lifetimes and insights into degradation mechanisms. This concept can be adapted to a wide range of electrochemical reactions and can be understood as an electrochemical turnover number known from the field of heterogeneous catalysis.

Moreover, in situ dissolution of various iridium-based oxides including highly crystalline, perovskite-based and amorphous structures over a wide range of current densities is presented. With regard to the severe leaching, observed for iridium-based perovskites in acidic electrolyte, explanations for the enhanced activity based on electronic interactions with rare-earth or alkali elements are debatable. The resulting amorphous iridium oxide, which is part of several studies on innovative OER materials<sup>1-4</sup>, shows exceptional high activity accompanied by high iridium dissolution. We demonstrate the participation of activated lattice oxygen atoms as a trigger for the boost in activity and the high dissolution rate due to the arising oxygen vacancies.

Based on our findings, future research in this field should be devoted to the formation of ultrathin films of crystalline iridium oxide on stable and conductive substrates with high surface area, such as fluorine-doped tin oxide, antimony-doped tin oxide or similar materials<sup>52</sup>. By doing so, the lower intrinsic activity and the fact

that exclusively the surface of crystalline iridium oxide is participating in the reaction could be compensated for. In the case that the superior activity of amorphous iridium oxides is utilized, stabilization of the weak iridium intermediate caused by oxygen vacancies will be of great importance. Further fundamental research in understanding the dissolution processes of amorphous iridium oxides will be essential to reach this goal.

## Methods

**Powder materials.**  $A_x\text{B}_y\text{IrO}_6$  ( $A = \text{Ba}$  or  $\text{Sr}$ ;  $B = \text{Pr}$ ,  $\text{Nd}$  or  $\text{Y}$ ) double perovskites were synthesized in alumina crucibles using  $\text{BaCO}_3$ ,  $\text{SrCO}_3$ ,  $\text{Pr}_6\text{O}_{11}$ ,  $\text{Nd}_2\text{O}_3$ ,  $\text{Y}_2\text{O}_3$  and metallic iridium powder, respectively. The standard solid-state reactions are described in the literature<sup>26</sup>. All reactions were carried out in air and the products were furnace-cooled to room temperature. The powders were intermittently reground during the synthesis. Amorphous iridium oxide (iridium (IV) oxide dihydrate) and crystalline iridium oxide (iridium (IV) oxide) were purchased from Alfa Aesar. To ensure complete crystallization, iridium (IV) oxide was additionally calcined at 600°C for 48 h in air.

For powder samples, the electrodes were prepared by drop-casting 0.3 µl suspension on a glassy carbon plate. All suspensions contained the same amount of iridium (0.27 mg ml<sup>-1</sup>). For some measurements of crystalline  $\text{IrO}_2$ , however, the concentration was enhanced to 4.5 mg ml<sup>-1</sup> to exceed the detection limit of the ICP-MS and measure reasonable currents in the CVs. To avoid detachment, 20 µl of Nafion solution (5 wt%, Sigma-Aldrich) was added to 5 ml of suspension. The dried spots ( $\varnothing \sim 1$  mm) were rinsed with water and located with the help of a vertical camera attached to the SFC. The measurements were carried out by placing the spot in the centre of the SFC's opening area ( $A = 0.035$  cm<sup>2</sup>).

**Film materials.** Ir metal films were deposited by physical vapour deposition in a magnetron sputter system (AJA ATC 2200-V) with a confocal target set-up. The 100-nm-thick Ir film was deposited on a thermally oxidized (1.5 µm  $\text{SiO}_2$ ) 4-inch-diameter Si (100) wafer with an intermediate, 10-nm-thick, Ti adhesion layer. Sputter targets were pre-cleaned at 150 W direct current (d.c.), 4 Pa, 300 s for Ti and 100 W d.c., 4 Pa, 30 s for Ir. The deposition was performed at 150 W d.c., 1.3 Pa, 150 s for Ti and 60 W d.c., 0.66 Pa, 1,200 s for Ir. Both layers were deposited with substrate rotation. The sputter system was operated with a base pressure  $< 2.6 \times 10^{-5}$  Pa and an Ar plasma.

For high current density measurements on iridium metal, lift-off photolithography was used to structure the thin film and create small catalyst dots (see Supplementary Methods and Supplementary Fig. 14). By doing so, the bubble detachment in the SFC was facilitated significantly. For the lift-off, a bilayer photoresist system consisting of an LOR20 B (MicroChem) bottom and an AZ 1518 (MicroChemicals) top layer was utilized. After deposition, the photoresist was removed in a cleaning cascade of acetone and isopropanol under ultrasonic agitation.

Hydrous  $\text{IrO}_x$  films were grown on the sputtered iridium spots by 300 square-wave pulses of 0.5 s between 0.05 V and 1.4 V versus the RHE.

Crystalline  $\text{IrO}_2$  films were produced on  $\text{Si}/\text{SiO}_2$  wafers via reactive sputtering in the presence of  $\text{O}_2$  using a d.c. magnetron sputtering machine (BesTech GmbH) followed by additional thermal treatment at 600°C for 48 h in air.

$\text{SrIrO}_3$  film samples were epitaxially grown using on-axis, radiofrequency magnetron sputtering of a  $\text{Sr}_4\text{IrO}_3$  target on (001)  $\text{SrTiO}_3$ . Due to two-dimensional growth, the surface of the samples was atomically flat, with 0.4 nm steps corresponding to the pseudo-cubic cell parameter. X-ray diffraction showed that the films were single crystals, oriented [110] perpendicular to the substrate<sup>53</sup>.

**Labelled samples.** Thin films of isotope-labelled reactively sputtered  $\text{Ir}^{18}\text{O}_2$  were deposited by magnetron sputtering (BesTech GmbH) at 100 W in a mixture of  $^{18}\text{O}_2$  (99.00 at.%, Sigma Aldrich) and Ar as the sputter gas and the chamber pressure was regulated to 0.5 Pa at room temperature. The base vacuum before deposition was  $2.0 \times 10^{-6}$  Pa. The  $\varnothing 3$  inch target of Ir (99.9%, Evochem) was pre-cleaned by sputtering against closed shutters before deposition. To prepare films with a minimal surface roughness, smooth substrates of single-crystalline Si(100) wafers with a 1.5 µm thermal  $\text{SiO}_2$  diffusion and reaction barrier layer were used. The resulting thickness of the obtained coating was approximately 80 nm. After the deposition, the films were annealed in vacuum at 500°C for 2 h. Unlabelled reactively sputtered  $\text{Ir}^{16}\text{O}_2$  was deposited using a mixture of  $^{16}\text{O}_2$  and Ar. All other conditions were kept as described before.

The  $^{18}\text{O}$ -labelled samples of hydrous  $\text{Ir}^{18}\text{O}_x$  were prepared using a solution of 0.1 M  $\text{HClO}_4$  in  $\text{H}_2^{18}\text{O}$  (97.76 at.%, Campro Scientific GmbH) applying a square-wave potential programme with upper and lower potential limits of 1.4 and 0.04 V versus the RHE, respectively (600 cycles at 0.5 Hz) to a sputtered Ir film (see description above). Afterwards the electrodes were carefully rinsed with ultrapure  $\text{H}_2^{16}\text{O}$  water and treated in a vacuum at 80°C for 2 h. Unlabelled samples were prepared using electrolyte containing 0.1 M  $\text{HClO}_4$  (Suprapur 70%  $\text{HClO}_4$ , Merck) in ultrapure  $\text{H}_2^{16}\text{O}$  water (PureLab Plus system, Elga, 18 MΩcm, total organic carbon (TOC)  $< 3$  ppb), using the same electrochemical programme.

All  $^{18}\text{O}$ -labelled samples were prepared right before the OLEMS measurements and transferred in a desiccator to avoid exchange of lattice oxygen in the topmost layers with air.

**Electrochemical measurements.** Dissolution measurements were performed in argon-purged 0.1 M  $\text{HClO}_4$  using a SFC connected to an ICP-MS<sup>54</sup>. A graphite rod and a Ag/AgCl electrode (Metrohm) were used as counter and reference electrodes, respectively. The electrolyte was prepared by dilution of concentrated acid (Suprapur 70%  $\text{HClO}_4$ , Merck) in ultrapure water (PureLab Plus system, Elga, 18 MΩcm, TOC  $< 3$  ppb). The flow rate through the cell was 352 µl min<sup>-1</sup>. Steady performance of the ICP-MS (NexION 300X, Perkin Elmer) was ensured by daily calibration and the addition of an internal standard solution downstream to the flow cell (measured isotopes:  $^{187}\text{Re}$ ,  $^{130}\text{In}$ ). A scheme of the SFC is presented in Supplementary Fig. 14.

OLEMS measurements were carried out using a SFC set-up, previously described elsewhere<sup>55</sup>. In contrast to the SFC connected to the ICP-MS, here the surface area of the working electrode was 0.125 cm<sup>2</sup> and a polytetrafluoroethylene tip was introduced from the top of the cell through an extra vertical channel. A 50-µm-thick polytetrafluoroethylene Gore-Tex membrane with a pore size of 20 nm, through which products can evaporate into the vacuum system of the mass spectrometer (Max 300 LG, Extrel), was mounted onto the very end of the tip. The approximate distance from the tip to the electrode was about 50 µm, which is determined by the thickness of the silicon ring sealing around the cell opening and the applied contact force. These parameters were kept constant during the whole set of measurements.

A potentiostat (Reference 600, Gamry) was used for the electrochemical measurements with both set-ups.

**Materials characterization.** Scanning electron microscopy measurements were performed in secondary electron mode using a Leo 1550 VP (Zeiss) operated at 15 kV and 6 mm sample distance. For energy-dispersive X-ray spectroscopy, the acceleration voltage was increased to 30 kV.

Measurements of x-ray photoelectron spectra were performed by applying a monochromatic Al K $\alpha$  X-ray source (1,486.6 eV) operating at 15 kV and 25 W (Quanter II, Physical Electronics). The binding energy scale was referenced to the C 1s signal at 285.0 eV.

Transmission electron microscopy (TEM) and SAED analyses were performed with a CM20 FEG electron microscope (from Philips) operated at 200 kV. The samples were prepared by drop-casting about 5 µl of catalyst suspension onto a gold TEM grid coated with a lacey carbon film (NH7, Plano GmbH).

**Lifetime calculation.** Lifetimes of the catalysts were calculated on the basis of equation (1):

$$t = \frac{S \times z \times F \times m}{j \times M} \quad (1)$$

where  $t$  is the lifetime of the catalyst (s),  $S$  is the stability number,  $z$  is the number of electrons per evolved  $\text{O}_2$ ,  $F$  is the Faraday constant (96,485 C mol<sup>-1</sup>),  $m$  is the loaded mass of iridium or any chosen element (g cm<sup>-2</sup>),  $j$  is the applied current density (A cm<sup>-2</sup>) and  $M$  is the molar mass of iridium or any chosen element (192.2 g mol<sup>-1</sup>).

**Data availability.** The authors declare that the main data supporting the findings of this study are available within the article and its Supplementary Information. Extra data are available from the corresponding authors upon request.

Received: 12 October 2017; Accepted: 26 April 2018;

Published online: 11 June 2018

## References

- Seitz, L. C. et al. A highly active and stable  $\text{IrO}_2/\text{SrIrO}_3$  catalyst for the oxygen evolution reaction. *Science* **353**, 1011–1014 (2016).
- Diaz-Morales, O. et al. Iridium-based double perovskites for efficient water oxidation in acid media. *Nat. Commun.* **7**, 12363 (2016).
- Reier, T. et al. Molecular insight in structure and activity of highly efficient, low-Ir Ir-Ni oxide catalysts for electrochemical water splitting (OER). *J. Am. Chem. Soc.* **137**, 13031–13040 (2015).
- Lettenmeier, P. et al. Nanosized  $\text{IrO}_2$ -Ir catalyst with relevant activity for anodes of proton exchange membrane electrolysis produced by a cost-effective procedure. *Angew. Chem. Int. Ed.* **55**, 742–746 (2016).
- Sun, W., Song, Y., Gong, X.-Q., Cao, L.-m. & Yang, J. An efficiently tuned  $d$ -orbital occupation of  $\text{IrO}_2$  by doping with Cu for enhancing the oxygen evolution reaction activity. *Chem. Sci.* **6**, 4993–4999 (2015).
- Sun, W. et al. OER activity manipulated by  $\text{IrO}_6$  coordination geometry: an insight from pyrochlore iridates. *Sci. Rep.* **6**, 38429 (2016).
- Nong, H. N. et al. Oxide-supported  $\text{IrNiO}_x$  core-shell particles as efficient, cost-effective, and stable catalysts for electrochemical water splitting. *Angew. Chem. Int. Ed.* **54**, 2975–2979 (2015).

8. Sun, W., Song, Y., Gong, X. Q., Cao, L. M. & Yang, J. Hollandite structure  $K_{0.25}IrO_2$  catalyst with highly efficient oxygen evolution reaction. *ACS Appl. Mater. Interfaces* **8**, 820–826 (2016).
9. Pourbaix, M. *Atlas of Electrochemical Equilibria in Aqueous Solutions* (National Association of Corrosion Engineers, 1974).
10. Geiger, S. et al. Activity and stability of electrochemically and thermally treated iridium for the oxygen evolution reaction. *J. Electrochem. Soc.* **163**, F3132–F3138 (2016).
11. Abbott, D. F. et al. Iridium oxide for the oxygen evolution reaction: correlation between particle size, morphology, and the surface hydroxo layer from operando XAS. *Chem. Mater.* **28**, 6591–6604 (2016).
12. Beni, G., Schiavone, L. M., Shay, J. L., Dautremont-Smith, W. C. & Schneider, B. S. Electrocatalytic oxygen evolution on reactively sputtered electrochromic iridium oxide films. *Nature* **282**, 281–283 (1979).
13. Bockris, J. O. M. & Otagawa, T. The electrocatalysis of oxygen evolution on perovskites. *J. Electrochem. Soc.* **131**, 290–302 (1984).
14. Suntivich, J., May, K. J., Gasteiger, H. A., Goodenough, J. B. & Shao-Horn, Y. A perovskite oxide optimized for oxygen evolution catalysis from molecular orbital principles. *Science* **334**, 1383–1385 (2011).
15. Zhu, L., Ran, R., Tadé, M., Wang, W. & Shao, Z. Perovskite materials in energy storage and conversion. *Asia-Pac. J. Chem. Eng.* **11**, 338–369 (2016).
16. Petrie, J. R., Jeen, H., Barron, S. C., Meyer, T. L. & Lee, H. N. Enhancing perovskite electrocatalysis through strain tuning of the oxygen deficiency. *J. Am. Chem. Soc.* **138**, 7252–7255 (2016).
17. May, K. J. et al. Influence of oxygen evolution during water oxidation on the surface of perovskite oxide catalysts. *J. Phys. Chem. Lett.* **3**, 3264–3270 (2012).
18. Risch, M. et al. Structural changes of cobalt-based perovskites upon water oxidation investigated by EXAFS. *J. Phys. Chem. C* **117**, 8628–8635 (2013).
19. Binninger, T. et al. Thermodynamic explanation of the universal correlation between oxygen evolution activity and corrosion of oxide catalysts. *Sci. Rep.* **5**, 12167 (2015).
20. Grimaud, A. et al. Activation of surface oxygen sites on an iridium-based model catalyst for the oxygen evolution reaction. *Nat. Energy* **2**, 16189 (2016).
21. Sen, F. G. et al. Towards accurate prediction of catalytic activity in  $IrO_2$  nanoclusters via first principles-based variable charge force field. *J. Mater. Chem. A* **3**, 18970–18982 (2015).
22. Gottesfeld, S. & Srinivasan, S. Electrochemical and optical studies of thick oxide layers on iridium and their electrocatalytic activities for the oxygen evolution reaction. *J. Electroanal. Chem. Interfacial Electrochem.* **86**, 89–104 (1978).
23. Reier, T., Weidinger, I., Hildebrandt, P., Kraehnert, R. & Strasser, P. Electrocatalytic oxygen evolution reaction on iridium oxide model film catalysts: influence of oxide type and catalyst substrate interactions. *ECS Trans.* **58**, 39–51 (2013).
24. Pfeifer, V. et al. The electronic structure of iridium and its oxides. *Surf. Interface Anal.* **48**, 261–273 (2016).
25. Sanchez Casalongue, H. G. et al. In situ observation of surface species on iridium oxide nanoparticles during the oxygen evolution reaction. *Angew. Chem. Int. Ed.* **53**, 7169–7172 (2014).
26. Fu, W. T. & Ijdo, D. J. W. On the space group of the double perovskite  $Ba_2PrIrO_6$ . *J. Solid State Chem.* **178**, 1312–1316 (2005).
27. Strasser, P. Free electrons to molecular bonds and back: closing the energetic oxygen reduction (ORR)–oxygen evolution (OER) cycle using core–shell nanoelectrocatalysts. *Acc. Chem. Res.* **49**, 2658–2668 (2016).
28. Cherevko, S. et al. Oxygen and hydrogen evolution reactions on Ru,  $RuO_2$ , Ir, and  $IrO_2$  thin film electrodes in acidic and alkaline electrolytes: a comparative study on activity and stability. *Catal. Today* **262**, 170–180 (2016).
29. Jovanović, P. et al. Electrochemical dissolution of iridium and iridium oxide particles in acidic media: transmission electron microscopy, electrochemical flow cell coupled to inductively coupled plasma mass spectrometry, and X-ray absorption spectroscopy study. *J. Am. Chem. Soc.* **139**, 12837–12846 (2017).
30. Trasatti, S. & Petrii, O. A. Real surface area measurements in electrochemistry. *J. Electroanal. Chem.* **327**, 353–376 (1992).
31. Minguzzi, A. et al. Easy accommodation of different oxidation states in iridium oxide nanoparticles with different hydration degree as water oxidation electrocatalysts. *ACS Catal.* **5**, 5104–5115 (2015).
32. Minguzzi, A. et al. Observing the oxidation state turnover in heterogeneous iridium-based water oxidation catalysts. *Chem. Sci.* **5**, 3591 (2014).
33. Pickup, P. G. & Birss, V. I. A model for anodic hydrous oxide growth at iridium. *J. Electroanal. Chem. Interfacial Electrochem.* **220**, 83–100 (1987).
34. Burke, L. D. & Whelan, D. P. A voltammetric investigation of the charge storage reactions of hydrous iridium oxide layers. *J. Electroanal. Chem. Interfacial Electrochem.* **162**, 121–141 (1984).
35. Fabbri, E., Haberer, A., Waltar, K., Kötz, R. & Schmidt, T. J. Developments and perspectives of oxide-based catalysts for the oxygen evolution reaction. *Catal. Sci. Technol.* **4**, 3800–3821 (2014).
36. Reier, T., Nong, H. N., Teschner, D., Schlögl, R. & Strasser, P. Electrocatalytic oxygen evolution reaction in acidic environments - reaction mechanisms and catalysts. *Adv. Energy Mater.* **7**, 1601275 (2016).
37. Rong, X., Parolin, J. & Kolpak, A. M. A fundamental relationship between reaction mechanism and stability in metal oxide catalysts for oxygen evolution. *ACS Catal.* **6**, 1153–1158 (2016).
38. Grimaud, A. et al. Activating lattice oxygen redox reactions in metal oxides to catalyse oxygen evolution. *Nature Chem.* **9**, 457–465 (2017).
39. Pfeifer, V. et al. Reactive oxygen species in iridium-based OER catalysts. *Chem. Sci.* **7**, 6791–6795 (2016).
40. Pfeifer, V. et al. In situ observation of reactive oxygen species forming on oxygen-evolving iridium surfaces. *Chem. Sci.* **8**, 2143–2149 (2017).
41. Willinger, E., Massue, C., Schlogl, R. & Willinger, M. G. Identifying key structural features of  $IrO_x$  water splitting catalysts. *J. Am. Chem. Soc.* **139**, 12093–12101 (2017).
42. Fierro, S., Nagel, T., Baltruschat, H. & Comminellis, C. Investigation of the oxygen evolution reaction on  $Ti/IrO_2$  electrodes using isotope labelling and on-line mass spectrometry. *Electrochem. Commun.* **9**, 1969–1974 (2007).
43. Rossmesl, J., Qu, Z. W., Zhu, H., Kroes, G. J. & Nørskov, J. K. Electrolysis of water on oxide surfaces. *J. Electroanal. Chem.* **607**, 83–89 (2007).
44. Ooka, H., Takashima, T., Yamaguchi, A., Hayashi, T. & Nakamura, R. Element strategy of oxygen evolution electrocatalysis based on in situ spectroelectrochemistry. *Chem. Commun.* **53**, 7149–7161 (2017).
45. Bockris, J. O. M. Kinetics of activation controlled consecutive electrochemical reactions: anodic evolution of oxygen. *J. Chem. Phys.* **24**, 817 (1956).
46. Cherevko, S. et al. Dissolution of noble metals during oxygen evolution in acidic media. *ChemCatChem* **6**, 2219–2223 (2014).
47. Mefford, J. T. et al. Water electrolysis on  $La_{1-x}Sr_xCoO_{3-\delta}$  perovskite electrocatalysts. *Nat. Commun.* **7**, 11053 (2016).
48. Cherevko, S., Geiger, S., Kasian, O., Mingers, A. & Mayrhofer, K. J. J. Oxygen evolution activity and stability of iridium in acidic media. Part 2. – Electrochemically grown hydrous iridium oxide. *J. Electroanal. Chem.* **774**, 102–110 (2016).
49. Kötz, R., Neff, H. & Stucki, S. Anodic iridium oxide films; XPS-studies of oxidation state changes and  $O_2$ -evolution. *J. Electrochem. Soc.* **131**, 72–77 (1984).
50. Kasian, O., Grote, J. P., Geiger, S., Cherevko, S. & Mayrhofer, K. J. J. The common intermediates of oxygen evolution and dissolution reactions during water electrolysis on iridium. *Angew. Chem. Int. Ed.* **57**, 2488–2491 (2018).
51. Kim, Y.-T. et al. Balancing activity, stability and conductivity of nanoporous core–shell iridium/iridium oxide oxygen evolution catalysts. *Nat. Commun.* **8**, 1449 (2017).
52. Oh, H.-S., Nong, H. N. & Strasser, P. Preparation of mesoporous Sb-, F-, and In-doped  $SnO_2$  bulk powder with high surface area for use as catalyst supports in electrolytic cells. *Adv. Funct. Mater.* **25**, 1074–1081 (2015).
53. Li, Z. Z., Schneegans, O. & Fruchter, L. Synthesis of perovskite  $SrIrO_3$  thin films by sputtering technique. Preprint at <http://arxiv.org/abs/1610.03722> (2016).
54. Klemm, S. O., Topalov, A. A., Laska, C. A. & Mayrhofer, K. J. J. Coupling of a high throughput microelectrochemical cell with online multielemental trace analysis by ICP-MS. *Electrochem. Commun.* **13**, 1533–1535 (2011).
55. Grote, J. P., Zeradjanin, A. R., Cherevko, S. & Mayrhofer, K. J. Coupling of a scanning flow cell with online electrochemical mass spectrometry for screening of reaction selectivity. *Rev. Sci. Instrum.* **85**, 104101 (2014).

## Acknowledgements

The authors acknowledge funding by the German Federal Ministry of Education and Research (BMBF) within the Kopernikus Project P2X and a further project (Kz: 033RC1101A). S.G. acknowledges financial support from BASF. O.K. acknowledges financial support from the Alexander von Humboldt Foundation. E.P. and T.O. acknowledge financial support from the IMPRS-SurMat doctoral program. K.J.J.M. acknowledges financial support from the DFG under project number MA4819/4-1. L.F. and Z.L. acknowledge support from the Agence Nationale de la Recherche grant SOCRATE ANR-15-CE30-0009-01. Additional thanks go to K. Hengge and T. Gänsler for carrying out the TEM and SAED measurements.

## Author contributions

S.G. composed the manuscript and performed electrochemical dissolution measurements. O.K. carried out OLEMS measurements,  $IrO_2$ -sputtering and XPS. A.M.M. carried out ICP-MS analysis. W.T.F. and O.D.-M. synthesized double-perovskite powders. Z.L. and L.F. synthesized  $SrIrO_3$  films. T.O. and A.L. contributed by allocating sputtered iridium dots. S.G., O.K., M.L., E.P., M.T.M.K., K.J.J.M. and S.C. contributed through scientific discussions and revision of the manuscript.

## Competing interests

The authors declare no competing interests.

## Additional information

Supplementary information is available for this paper at <https://doi.org/10.1038/s41929-018-0085-6>.

Reprints and permissions information is available at [www.nature.com/reprints](http://www.nature.com/reprints).

Correspondence and requests for materials should be addressed to S.G. or S.C.

**Publisher's note:** Springer Nature remains neutral with regard to jurisdictional claims in published maps and institutional affiliations.